

RESEARCH ARTICLE | JULY 01 2024

Modeling interactions between rubidium atom and magnetometer cell wall molecules

Grégoire David  ; Andrew M. Wibowo-Teale  ; David M. Rogers  



J. Chem. Phys. 161, 014301 (2024)

<https://doi.org/10.1063/5.0201903>



APL Energy

Latest Articles Online!

Read Now



Modeling interactions between rubidium atom and magnetometer cell wall molecules

Cite as: J. Chem. Phys. 161, 014301 (2024); doi: 10.1063/5.0201903

Submitted: 1 February 2024 • Accepted: 17 June 2024 •

Published Online: 1 July 2024



View Online



Export Citation



CrossMark

Grégoire David,^{a)}  Andrew M. Wibowo-Teale,^{b)}  and David M. Rogers^{b)} 

AFFILIATIONS

School of Chemistry, University of Nottingham, University Park, Nottingham NG7 2RD, United Kingdom

^{a)}Univ Rennes, CNRS, ISCR (Institut des Sciences Chimiques de Rennes)-UMR 6226, F-35000 Rennes, France.

^{b)}Author to whom correspondence should be addressed: david.rogers@nottingham.ac.uk

ABSTRACT

Magnetometer cell wall coat molecules play an important role in preserving the lifetime of pumped alkali metal atoms for use in magnetometers that are capable of measuring very small magnetic fields. The goal of this study is to help rationalize the design of the cell coat molecules. Rubidium-87 is studied in terms of its interaction with three template cell coat molecules: ethane, ethene, and methyltrichlorosilane (MeTS). *Ab initio* electronic structure methods are applied to investigate the effect that the coat molecules have on the 2S ground state and 2P excited state of ^{87}Rb . We find that, from the *ab initio* results, the three template molecules have differing effects, with MeTS having the largest effect on the ground state and ethane or ethene having the largest effect on the non-degenerate excited states.

© 2024 Author(s). All article content, except where otherwise noted, is licensed under a Creative Commons Attribution-NonCommercial 4.0 International (CC BY-NC) license (<https://creativecommons.org/licenses/by-nc/4.0/>). <https://doi.org/10.1063/5.0201903>

I. INTRODUCTION

Atomic magnetometers are used for sensing very small magnetic fields (down to ~ 1 femto Tesla), where applications include biological imaging, geology, global positioning, and fundamental experiments.^{1,2} An all-optical atomic magnetometer operates as follows:¹ (i) A vapor of alkali atoms (K, Rb, or Cs) within a glass vapor cell has randomly orientated atomic spins; (ii) circularly polarized pump light aligns the spins with the pump beam, and when a small magnetic field is applied, the spins precess in the magnetic field; (iii) the orientated spins rotate the polarization of linearly polarized probe light (Faraday rotation); and (iv) the intensity or polarization of the transmitted probe light measures the magnetic field strength. An anti-relaxation coat on the cell walls preserves the spin polarization (lifetime) of the alkali atoms. A key feature is the importance of designing cell wall coatings with good relaxation properties for these experiments. For a comprehensive discussion of alkali-metal vapor cells and anti-relaxation coatings, including surface fabrication and characterization techniques, the reader is referred to the review of Chi *et al.*³ Moreover, Wu has reviewed the progress that has been made over the past six decades in understanding the nature of the wall interactions of spin-polarized atoms.⁴

In a spin-exchange relaxation-free (SERF) magnetometer,⁵ pumped alkali atoms are in an excited state with hyperfine level

F' . As an example, the D_1 line ($5^2S_{1/2}$ to $5^2P_{1/2}$ transition) in ^{87}Rb was used to directly measure the average dwell time of spin polarized rubidium atoms on coated glass surfaces.⁶ The $F = 1$ to $F' = 1, 2$ transition (optical pump) creates spin polarization in the Zeeman multiplets (M_F) of the ground state $F = 2$ hyperfine level. Probe light tuned to the $F = 2$ to $F' = 1, 2$ transition (D_1 line) probes the population in the $F = 2$ state. The spin polarization is monitored by the rotation of the polarization plane (Faraday rotation) of the probe beam. When two spin polarized atoms collide, the electrons can transition into the other hyperfine state, or precess (change in orientation of the rotational axis) in the opposite direction from the bulk of the ensemble, thereby causing decoherence and loss of signal. Spin-exchange relaxation is suppressed if collisions occur fast enough in low magnetic fields. In such a regime, the spins do not have enough time to precess and decohere between collisions. This is achieved by operating with a sufficiently high alkali metal density (at a higher temperature) and in sufficiently low magnetic fields. Collisions with the cell walls also result in spin decoherence, which is minimized by the vapor cell wall coating.

It has long been recognized that paraffin ($\text{C}_n\text{H}_{2n+2}$, where $n > 20$) is a good coat molecule for magnetometer cell walls.⁷ Alternative coat molecules to paraffin include alkyl chains terminated with the functional group trichlorosilane (organochlorosilanes)⁶ and mono-unsaturated alkene chains.⁸

Ulanski and Wu measured dwell times of spin polarized rubidium-87 atoms on pentacontane ($\text{CH}_3(\text{CH}_2)_{48}\text{CH}_3$) and octadecyltrichlorosilane (OTS) coated surfaces.⁶ They used the Larmor frequency shift of ^{87}Rb to determine, at 72 °C, the dwell times in OTS-coated cells as 0.9 μs and in paraffin-coated cells as 1.8 μs . The dwell time for OTS is shorter than that for paraffin, whereas the relaxation probability for OTS is larger than that for paraffin by almost one order of magnitude: paraffin-coated surfaces can support 10 000 polarization-preserving collisions with spin-polarized Rb atoms;⁷ in contrast, OTS-coated surfaces can support 1000 collisions.^{9,10} They concluded that the superior anti-relaxation property of paraffin is not due to the extremely short dwell time of spin polarized ^{87}Rb atoms in paraffin-coated cells but rather to the average strength of the interactions experienced by the atoms while they are inside paraffin-coated cells, which are much weaker than while they are inside OTS-coated cells.

Corsini *et al.* measured for the D_1 transition in ^{85}Rb and ^{87}Rb hyperfine frequency shifts and spin relaxation times with saturated alkane and mono-unsaturated alkene cell coats.⁸ It was assumed that the hyperfine frequency shift is proportional to cell-wall dwell time (and adsorption energy). For ^{87}Rb with a paraffin and an alkene (C20–24) coat in spherical cells at 21 and 28 °C, respectively, hyperfine frequency shifts (and spin relaxation times) of -57 Hz (3.5 s) and -83 Hz (17.7 s) were observed. It was concluded that spin relaxation time depends not on the cell-wall dwelling time but on a smaller RMS magnitude of the average spatial fluctuations of the cell-wall adsorption energy.

Atomic force microscopy (AFM) has been used by Dong *et al.*¹¹ to study energy dissipation on the surface coating of a magnetometer cell wall, where the energy dissipation between the AFM tip and the surface coating is assumed to be approximately equal to the adsorption energy induced by the collision between alkali-metal atoms and the surface coating. They established that the energy dissipation on the coating (paraffin) of the cell surface is related to the relaxation rate of the alkali-metal (Cs atom) vapor cell. The energy dissipation is directly proportional to the square root of the relaxation rate (or inversely proportional to the square root of relaxation time). Thus, showing that the anti-relaxation behavior of the cell wall coating can be characterized by the energy dissipation on the coating. Hence, the performance of anti-relaxation coatings on alkali-metal cells can be directly analyzed using the energy dissipation of anti-relaxation coatings instead of measuring the relaxation time. Therefore, characterizing the atomic and molecular interactions between alkali metal atoms and surface coatings may help to understand the adsorption energy and the energy dissipation.

Each of these studies, therefore, suggests that the specific interactions between the alkali metal atoms and the surface coating molecules may be key to understanding how the choice of coating influences magnetometer cell performance. In this work, we present *ab initio* quantum chemical computations to study the interactions between an alkali atom and cell wall coat molecules that aim to help rationalize the design and fabrication of magnetometer cell coats. We consider the template molecules ethane (to represent an alkane), ethene (an alkene), and methyltrichlorosilane (MeTS) (an organochlorosilane). The purpose of this study is to aid in the design of a better and more consistently applied cell coat than a saturated alkyl chain that can be easily fabricated and that would be stable at high temperatures, a characteristic desired for SERF magnetometers.

In this study, we focus on the ground state (5^2S) and three degenerate excited states (5^2P) of ^{87}Rb . In particular, we study the effect of the electric field due to the coat molecule on the ground and the excited states of ^{87}Rb .

II. METHODS

Ground state ^{87}Rb -coat-molecule structures were optimized at the MP2 level of theory with the def2-TZVP basis set,^{12,13} with an effective-core-potential (ECP) for a Rb atom, using Gaussian 16 Rev. A.03.¹⁴ OpenMolcas¹⁵ was employed to perform state-averaged CASSCF and CASPT2 calculations on the lowest energy ground state structures and potential energy scans along the coordinate between ^{87}Rb and each coat molecule. The Sapporo TZP 2012 all-electron basis set^{16–18} was used for the CASSCF and CASPT2 calculations. The CASSCF active space comprises the 5s orbital and electron and the three 5p orbitals on ^{87}Rb and is denoted (1, 4). This minimal active space is able to describe the ground state (5^2S) and the three degenerate excited states (5^2P) of ^{87}Rb . State-averaged CASSCF calculations for the four lowest-energy roots in C_1 symmetry were performed throughout this study. The CASPT2 calculations employed an IP-EA level-shift of 0.25 hartree. The electric field (and gradient) was evaluated using the “FLDG = 0” keyword in OpenMolcas. The electric field was evaluated for each state, where the plots in Figs. 3–7 are for the ground and excited state properties vs ground-state electric fields only. The electric field includes the effects of the electronic charge density shifts of the ^{87}Rb atom due to the interactions with the cell coating molecules. Spin-orbit coupling (SOC) was described using the RASSI program within OpenMolcas to compute the spin-orbit coupled states using single-state (SS) CASPT2 energies for the spin-free effective Hamiltonian's diagonal elements.

III. RESULTS AND DISCUSSION

For the isolated ^{87}Rb atom, the transition energy from the 5^2S ground state to the 5^2P excited state is predicted to be at 1.488 eV at the CASPT2/TZP level of theory. This can be compared with the experimental values of 1.560 and 1.589 eV for the D_1 ($5^2\text{S}_{1/2}$ to $5^2\text{P}_{1/2}$) and D_2 ($5^2\text{S}_{1/2}$ to $5^2\text{P}_{3/2}$) transitions, respectively.^{19,20} Taking spin-orbit coupling into account for an isolated atom of ^{87}Rb using SS-CASPT2/TZP energies, the transition energy for D_1 is at 1.476 eV, with the D_2 transition energy at 1.494 eV. One conformation for each of the ^{87}Rb -coat-molecules is considered and is the lowest energy conformer, with no imaginary harmonic vibrational frequencies, of those we found at the MP2/def2-TZVP level for ^{87}Rb -ethane (two conformers), ^{87}Rb -ethene (three conformers), and ^{87}Rb -MeTS (three conformers). Figure 1 displays their optimized structures, and their Cartesian coordinates are available in the supplementary material. For each system, constrained potential energy scans were performed in 0.2 Å intervals along the coordinate between ^{87}Rb and the coat molecule. The distance to the ^{87}Rb atom is from the CC bond midpoint in ethane and ethene and the plane of the three Cl atoms in MeTS. The electronic states of ^{87}Rb in the environment of the coat molecule are labeled as 1^2A for the ground state (5^2S) and 2^2A , 3^2A , and 4^2A for the three excited states (5^2P), one for each Cartesian component or azimuthal quantum number of the 5p orbital, and in ascending order of energy.

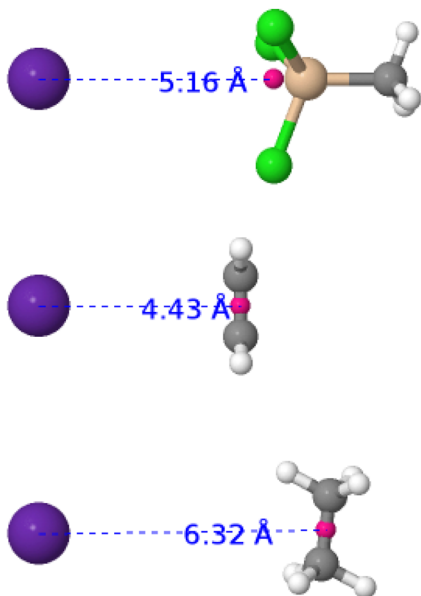


FIG. 1. Optimized geometries for ^{87}Rb with ethane (bottom), ethene (middle), and MeTS (top) at the MP2/def2-TZVP level. The coordinate connecting ^{87}Rb to the coat molecule is shown as a dashed blue line with the point on the coat molecule in magenta, with the optimized distance shown in angstroms.

First, we consider the electric field (E), due to the coat molecule, that a ^{87}Rb atom (that is, the atomic coordinate of the ^{87}Rb nucleus) would experience at a given distance. Figure 2 displays the *ab initio* computations (CASPT2/TZP) of the norm of the electric field ($\|\vec{E}\|$) felt at the ^{87}Rb atom as a function of the distance with ethane, ethene,

and MeTS [Fig. 2(a)], and the distance between the ^{87}Rb atom and ethane, ethene, and MeTS as a function of the norm of the electric field felt by the ^{87}Rb atom [Fig. 2(b)]. As shown in the plots, MeTS (green curve) has the largest spatially extended E , followed by ethene (red curve), and ethane (blue curve), where the strength of the field at short distances is weaker for ethene, which reaches a peak around 3.5 Å [Fig. 2(a)]. This is confirmed in Fig. 2(b), where an incoming atom would experience the strongest field due to MeTS. ^{87}Rb -MeTS has the largest dipole moment of the three coat molecules with ^{87}Rb (Table S4). The MP2/def2-TZVP dipole moment magnitudes for the optimized geometries of ^{87}Rb -MeTS, ^{87}Rb -ethene, and ^{87}Rb -ethane are, respectively, 3.6794, 2.3550, and 0.2282 D. In all cases, the largest component is along the ^{87}Rb -molecule coordinate. These dipole moment magnitudes are in line with the norm of the electric field for MeTS, ethene, and ethane (Fig. 2).

We now consider the ground 5^2S and 5^2P excited states of ^{87}Rb upon interaction with each of the template coat molecules. The results of the *ab initio* computations are described, and based on the $\|\vec{E}\|$ plots, we focus on the inter-species distances of >4.0 Å, where the E strength is comparable for each coat molecule and of a relatively small magnitude. The minima on the ground state potential energy surfaces are around 4.0 Å, and at shorter distances, there are strongly repulsive interactions between ^{87}Rb and each coat molecule. Along the coordinate between ^{87}Rb and each coat molecule, potential energy scans, energy shifts (energy at distance R minus dissociated energy for each state, i.e., the interaction energy for each state relative to dissociation products) as a function of ground-state $\|\vec{E}\|$, and vertical transition energies as a function of ground-state $\|\vec{E}\|$ at the CASPT2/TZP level of theory are discussed.

A. Ethane

Figure 3 displays potential energy scans along the ^{87}Rb -ethane distance [Fig. 3(a)], energy shifts (energy at distance R minus

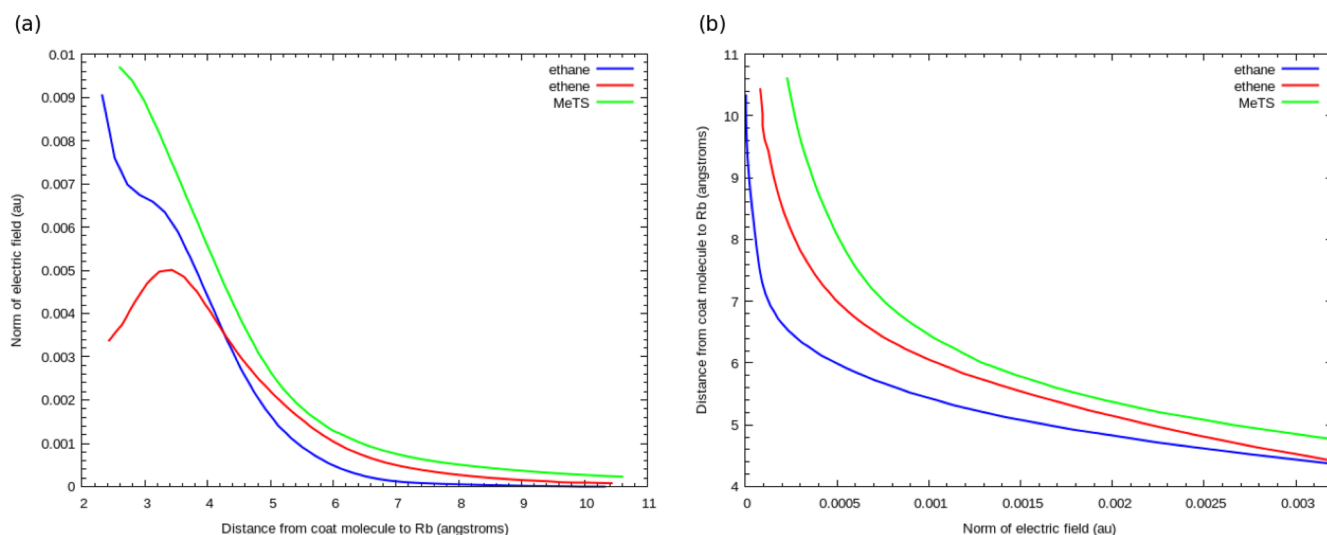


FIG. 2. (a) Norm of the electric field for the ground state of ^{87}Rb with ethane, ethene, and MeTS at the CASPT2/TZP level experienced at various distances by ^{87}Rb . Norm of the electric field ($\|\vec{E}\|$) felt at the ^{87}Rb atom as a function of the distance with ethane (blue), ethene (red), and MeTS (green). (b) The distance between the ^{87}Rb atom and ethane (blue), ethene (red), and MeTS (green) as a function of the norm of the electric field felt by the ^{87}Rb atom.

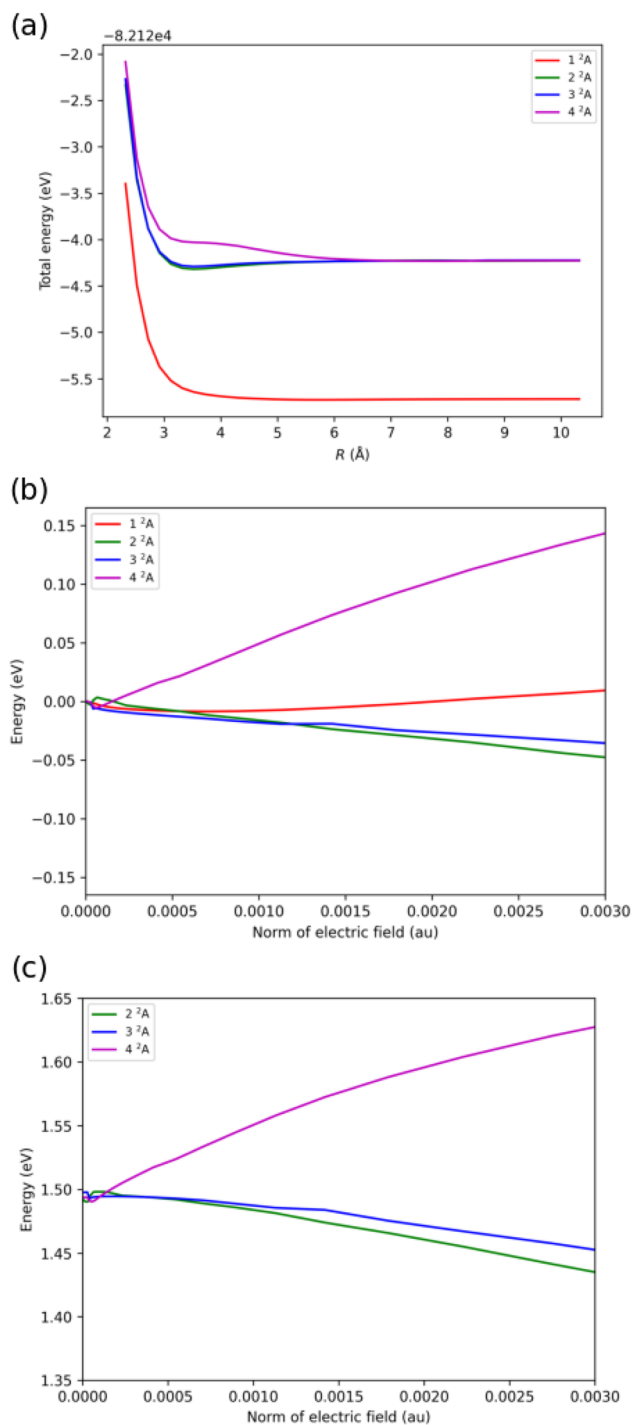


FIG. 3. (a) CASPT2/TZP potential energy scan of ^{87}Rb with ethane. (b) CASPT2/TZP energy shift as a function of ground-state $||\vec{E}||$. (c) CASPT2/TZP transition energy as a function of ground-state $||\vec{E}||$.

dissociated energy for each state) as a function of ground-state $||\vec{E}||$ [Fig. 3(b)], and vertical transition energies as a function of ground-state $||\vec{E}||$ [Fig. 3(c)], all at the CASPT2/TZP level of theory. Figure 3(a) shows very shallow energy minima for the ground state and two of the non-degenerate excited states (blue and green curves), with the third higher-lying excited state being repulsive (magenta curve). The two excited states with shallow minima involve p-type orbitals orthogonal to the coordinate between ^{87}Rb -ethane, whereas the higher-energy third excited state involves a p-type orbital that lies along the inter-species distance. The energy shifts [Fig. 3(b)] show that the two excited states with a p-type orbital orthogonal to the coordinate of the ethane molecule are stabilized (undergo a negative shift), whereas the third excited state is destabilized (undergoes a positive shift). The energy shift for the ground state is predicted to decrease slightly and then increase. The transition energies [Fig. 3(c)] echo the preceding plot and show that the two excited states with a p-type orbital orthogonal to the axis of the ethane molecule are stabilized, whereas the third excited state is destabilized.

B. Ethene

Figure 4 displays potential energy scans [Fig. 4(a)], energy shifts [Fig. 4(b)], and transition energies [Fig. 4(c)] with respect to $||\vec{E}||$ at the CASPT2/TZP level for ^{87}Rb -ethene. Figure 4(a) shows more pronounced energy minima of around 3.3 Å for the two lower-lying excited states (green and blue curves), with the third higher-lying excited state having a shallower minimum and a repulsive profile at an inter-species distance of greater than 4.5 Å (magenta curve). The energy shifts [Fig. 4(b)] with respect to $||\vec{E}||$ show that the two excited states with a p-type orbital orthogonal to the axis of the ethene molecule are stabilized by the external field, whereas the third excited state, with a p-type orbital along the plane of interaction, is destabilized. The energy shift for the ground state is predicted to decrease slightly and then remain stationary. The transition energies [Fig. 4(c)] echo the preceding plot and show that the two excited states with a p-type orbital orthogonal to the field (the coordinate to the ethene molecule) are stabilized, whereas the third excited state is destabilized. For the energy shifts and the transition energies, the shifts when the E is applied are greater for ^{87}Rb with ethene than for ^{87}Rb with ethane, with the exception of the energy shift and transition energy for the third excited state, which undergoes a larger blue-shift in the presence of ethane. The difference in energy between the two low-lying ^{87}Rb p-type orbitals in ^{87}Rb -ethene is more pronounced and is due to one of the low-lying p-type orbitals lying along the axis of ethene (C=C), with the other low-lying p-type orbital lying across the axis of ethene. The 2^2A state has the ^{87}Rb p-type orbital $5p_y$ lying along the ethene axis (C=C) and has the lower transition energy, with the $5p_x$ orbital lying across C=C, and that state, 3^2A , has the higher transition energy of the two states.

C. MeTS

Figure 5 displays potential energy scans [Fig. 5(a)], energy shifts [Fig. 5(b)], and transition energies [Fig. 5(c)] with respect to $||\vec{E}||$,

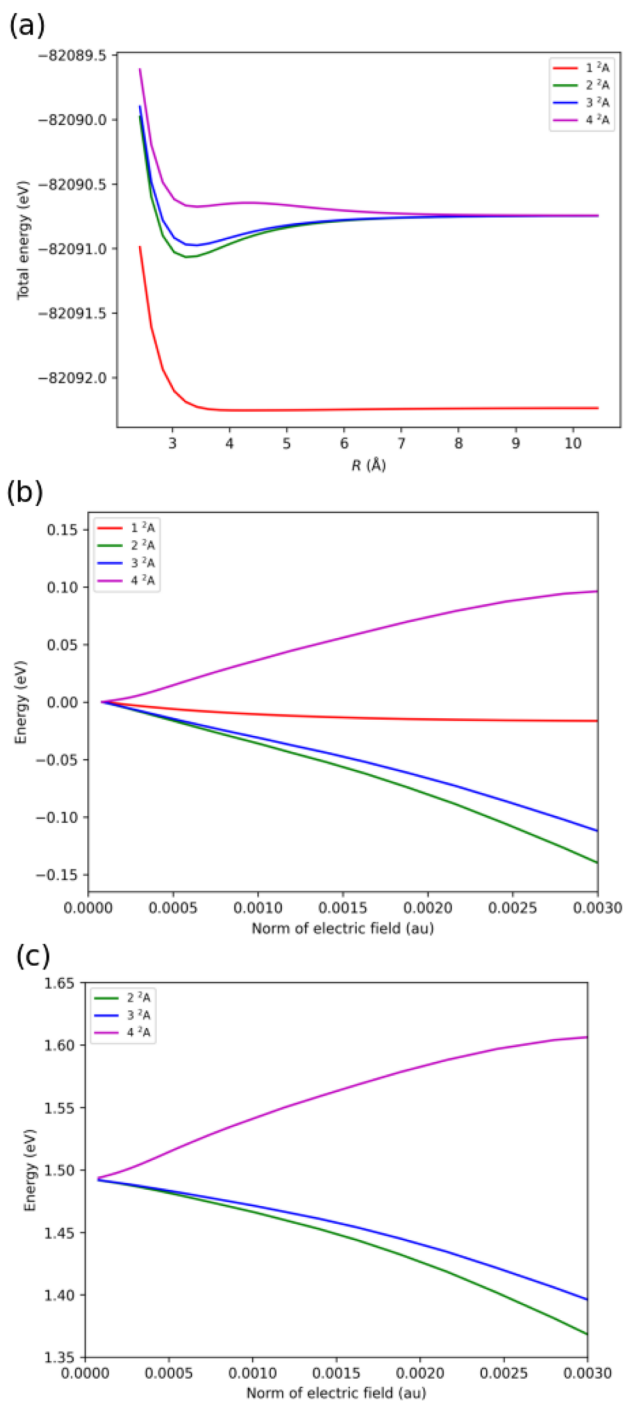


FIG. 4. (a) CASPT2/TZP potential energy scan of ^{87}Rb with ethene. (b) CASPT2/TZP energy shift as a function of ground-state $||\vec{E}||$. (c) CASPT2/TZP transition energy as a function of ground-state $||\vec{E}||$.

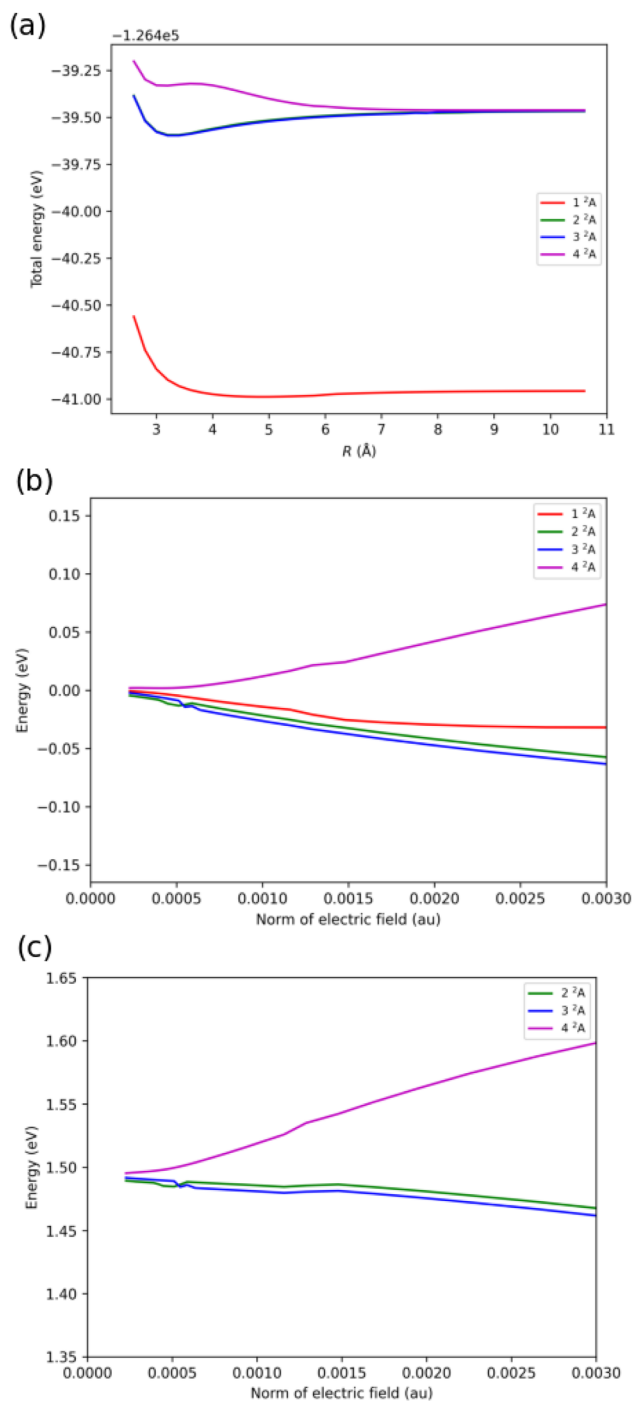


FIG. 5. (a) CASPT2/TZP potential energy scan of ^{87}Rb with MeTS. (b) CASPT2/TZP energy shift as a function of ground-state $||\vec{E}||$. (c) CASPT2/TZP transition energy as a function of ground-state $||\vec{E}||$.

at the CASPT2/TZP level for ^{87}Rb -MeTS. Figure 5(a) shows pronounced energy minima of around 3.2 Å for the two lower-lying excited states, with the third higher-lying excited state having a shallower minimum and a repulsive profile at an inter-species distance of greater than 3.8 Å. The ground state energy profile has a very shallow minimum of around 5.0 Å. The energy shifts [Fig. 5(b)] show that the two excited states with a p-type orbital orthogonal to the axis of the MeTS molecule are stabilized, whereas the third excited state, with a p-type orbital along the plane of interaction, is destabilized. The energy shift for the ground state is predicted to decrease and then remain stationary. The transition energies [Fig. 5(c)] echo the preceding plot and show that the two excited states with a p-type orbital orthogonal to the coordinate of the MeTS molecule are stabilized, whereas the third excited state is destabilized.

D. Comparison of template coat molecules

Figure 6 presents energy shifts of the ground and the three excited states as a function of ground-state $\|\vec{E}\|$ [Fig. 6(a)], and transition energies as a function of ground-state $\|\vec{E}\|$ [Fig. 6(b)] for the three template coat molecules with ^{87}Rb . For the energy shifts of the ground 5^2S state (1^2A) of ^{87}Rb as a function of ground-state $\|\vec{E}\|$, the shift is greatest for MeTS, followed by ethene, and then ethane [Fig. 6(a)]. For the two lower-lying excited states, 2^2A and 3^2A , the negative shifts are the greatest for ethene, followed by MeTS, and then ethane (in red, green, and blue, respectively). The third and higher-lying excited state, 4^2A , undergoes a positive shift, with the largest shift with ethane, followed by ethene, and then MeTS. The transition energies to the three 5^2P excited states of ^{87}Rb follow similar trends, with the transition energies to the two lower-lying excited states undergoing the largest negative shifts with ethene, followed by ethane, and then by MeTS [Fig. 6(b)]. At $\|\vec{E}\| \leq 0.0015$ au, the shifts due to ethane are comparable to MeTS. For the third higher-lying excited state, the greatest positive shift is predicted for ^{87}Rb inter-

acting with ethane, followed by ethene and then MeTS. The above discussion for each coat template molecule indicates that the two lower-lying excited states of ^{87}Rb (with a p-type orbital orthogonal to the axis of interaction) are stabilized in the electric field of the coat molecule, whereas the third higher-lying excited state (with a p-type orbital along the axis of interaction) is destabilized.

Despite having the largest magnitude for the E, the ^{87}Rb -MeTS system is predicted by the *ab initio* computations to have the greatest effect on only the energy shift of the ground state of ^{87}Rb , with ethene or ethane having the largest effect on the excited state. This suggests that the magnitude of E along the approach coordinate is not the decisive factor for how the electronic states are influenced, but rather the differences in the local non-uniformity of E for the different coat molecules. The form of the curves plotted of energy shift and transition energy vs $\|\vec{E}\|$ [Figs. 6(a) and 6(b), respectively] resemble a Stark effect, where the wavelength of light emitted/absorbed by an atom is altered by the application of a transverse electric field to the polarization of the light source.

The above discussion considered the energies, energy shifts, and transition energies with respect to the norm of the electric field. Coupling between the quadrupole moment of the electronic states of ^{87}Rb and the electric field gradient of the coat molecules is expected to shift the energy of the electronic states. Figures S1–S3 display plots of CASPT2/TZP energy shift for the four electronic states vs ground-state CASPT2/TZP electric field gradient (EFG) for three anisotropic terms for ^{87}Rb with each coat molecule. For ^{87}Rb with ethane and magnitudes of the EFG < 0.3 au [$(2YY - ZZ - XX)/2$ for the coordinate along the axis of interaction and $R > 3.0$ Å], the 4^2A and 1^2A states undergo a positive energy shift, whereas the 2^2A and 3^2A states undergo a negative energy shift of nearly equal magnitude to each other. For ^{87}Rb with ethene and magnitudes of the EFG < 0.8 au [$(2ZZ - XX - YY)/2$ for the coordinate along the axis of interaction and $R > 2.8$ Å], the 4^2A and 1^2A states undergo a positive energy shift, whereas the 2^2A and 3^2A states undergo a negative energy

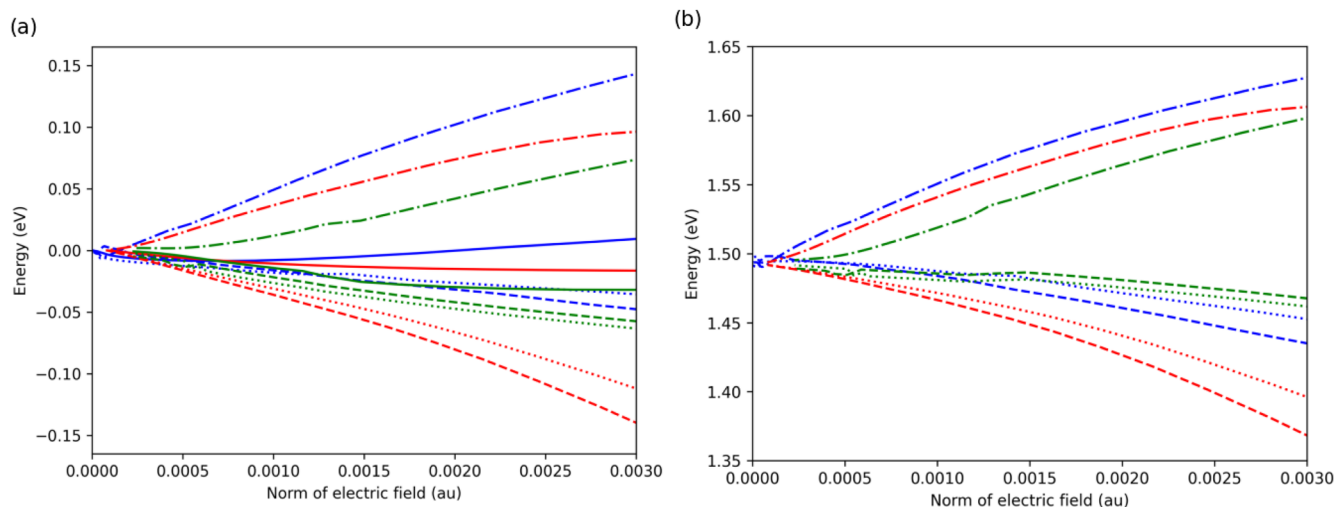


FIG. 6. (a) CASPT2/TZP energy shift of the ground state and the three excited states as a function of ground-state $\|\vec{E}\|$, and (b) transition energy as a function of ground-state $\|\vec{E}\|$. ^{87}Rb with ethane (blue), ethene (red), and MeTS (green). State 1^2A (solid line), state 2^2A (dashed line), state 3^2A (dotted line), and state 4^2A (dashed-dotted line).

TABLE I. Adsorption energy (eV) for ^{87}Rb with the three template coat molecules. Energy computed from the potential energy curves at the CASPT2/TZP level. For ^{87}Rb -ethane, there is no physisorbed minimum for state 4^1A ; therefore, this energy was taken at a distance of 3.52 \AA that was used for the 2^1A and 3^1A states.

State	Adsorption energy (eV)		
	^{87}Rb -ethane	^{87}Rb -ethene	^{87}Rb -MeTS
1^1A	-0.009	-0.017	-0.032
2^1A	-0.090	-0.321	-0.131
3^1A	-0.068	-0.230	-0.134
4^1A	0.197	0.068	0.133

shift, where the 2^2A state experiences a larger negative shift than the 3^2A state. For ^{87}Rb with MeTS and magnitudes of the EFG $< 0.225 \text{ au}$ [$(2XX - YY - ZZ)/2$ for the coordinate along the axis of interaction and $R > 2.8 \text{ \AA}$], the 4^2A state undergoes a positive shift, and the 1^2A state undergoes a negative shift that becomes a positive shift at around an EFG of 0.05 au . The 2^2A and 3^2A states for ^{87}Rb with MeTS undergo a negative energy shift of nearly equal magnitude.

The lowering of the ground 1^2A state follows coat molecules MeTS $>$ ethene $>$ ethane, where 1^2A has undergone the largest (negative) shift for MeTS [Fig. 6(a)]. This may be a result of the favorable interaction between ^{87}Rb and MeTS that leads to a very shallow and broad potential energy curve for ground-state 1^2A [Fig. 5(a)] and the largest relative negative adsorption energy (Table I). The adsorption energy for the ground state follows the trend MeTS $>$ ethene $>$ ethane.

E. Spin-orbit coupling

For the isolated ^{87}Rb atom, the energy splitting of the $5^2\text{P}_{1/2}$ and $5^2\text{P}_{3/2}$ J levels is calculated to be 0.018 eV using SS-CASPT2/TZP

energies in the computation of SOC. The experimental splitting is 0.029 eV .^{19,20} Thus, it is judicious to assess the impact of SOC on the energy shifts and transition energies discussed above. Figure 7 presents energy shifts of the ground and the three excited states as a function of ground-state $\|\vec{E}\|$ [Fig. 7(a)], and transition energies as a function of ground-state $\|\vec{E}\|$ [Fig. 7(b)] for the three template coat molecules with ^{87}Rb when SOC is taken into account. As found for the non-SOC computed energy shifts, the ^{87}Rb SOC 4^2A state undergoes a positive energy shift and follows the trend of coat molecule ethane $>$ ethene $>$ MeTS. The energy shift of the ^{87}Rb SOC ground state (1^2A) follows MeTS $>$ ethene $>$ ethane, as noted for the non-SOC ground state, with both MeTS and ethene giving a negative energy shift. The SOC 2^2A and 3^2A states of ^{87}Rb all undergo negative shifts with slightly different magnitudes compared to the non-SOC 2^2A and 3^2A states. For the SOC 2^2A and 3^2A states of ^{87}Rb , the largest negative shifts are for interaction with the ethene coat, as found for the non-SOC states. A similar trend is found for the transition energies of the SOC states of ^{87}Rb when interacting with the coat molecules, where the 4^2A state undergoes a blue shift and the 2^2A and 3^2A states shift to the red as the magnitude of the electric field increases. For each system at large ^{87}Rb -coat-molecule separation, R , the SOC 2^2A state lies lower in energy (by $\sim 0.02 \text{ eV}$) than the SOC 3^2A and 4^2A states, where the latter two states are very close in energy.

IV. CONCLUSIONS

We have studied the effect of three template coat molecules on the ground 5^2S and 5^2P excited states of ^{87}Rb . We studied the interaction between the coat molecules and ^{87}Rb in terms of the ground state electric field at various inter-species distances. We found that the coat molecules influence the energy shifts (energy at distance R minus dissociated energy for each state) and vertical transition energies to different degrees. The energy shift of the ground

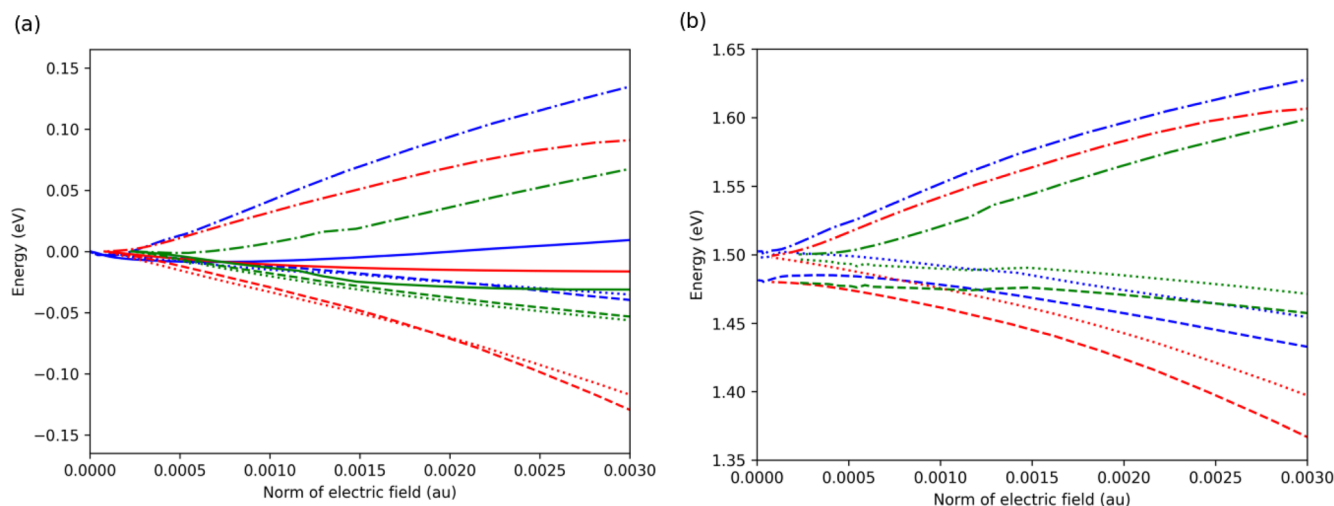


FIG. 7. (a) Energy shift of the spin-orbit coupled (SOC) electronic states as a function of ground-state $\|\vec{E}\|$, and (b) transition energy as a function of ground-state $\|\vec{E}\|$. SS-CASPT2/TZP energies were used for the spin-free effective Hamiltonian's diagonal elements. ^{87}Rb with ethane (blue), ethene (red), and MeTS (green). State 1^2A (solid line), state 2^2A (dashed line), state 3^2A (dotted line), and state 4^2A (dashed-dotted line).

state is affected by the three coat molecules in rank MeTS > ethene > ethane. The energy shifts and transition energies of the excited state show that it is split into two lower- and one higher-lying states, with the former being stabilized (red-shifted) and the latter destabilized (blue-shifted). The ethene coat stabilizes the lower two states to the largest extent; the ethane coat destabilizes the third state to the largest extent. The character and magnitude of the energy splitting may have a bearing on the design of magnetometer cell coats in terms of the interaction with a pumped state of ^{87}Rb (or another alkali atom) and its lifetime.

The *ab initio* computations suggest that transitions to a stabilized state (with a p-type orbital perpendicular to the coordinate to the coat molecule) may lead to a shorter lifetime for an ensemble of ^{87}Rb atoms than transitions to a destabilized state (with a p-type orbital parallel to the coordinate to the coat molecule); the stabilized atomic states have a negative interaction energy with the coat molecules (i.e., favorable physisorption for a bound species) and, therefore, a larger rate of decoherence, whereas the destabilized states have a positive interaction energy (unfavorable physisorption). The computed adsorption energies are shown in Table I. The population of the destabilized state would preserve the spin polarization by avoiding collisions with the cell wall coat, which leads to decoherence, as the destabilized state cannot physisorb onto the cell wall coat.

This observation from the *ab initio* computations is in line with the experimental results. Dong *et al.*¹¹ have observed that for a Cs atom interacting with a surface coating of paraffin, the energy dissipation (\approx adsorption energy) is directly proportional to the square root of the relaxation rate or inversely proportional to the square root of relaxation time. In addition, the interaction with the cell wall coat is considered dominant over cell-wall dwell time; for example, when comparing paraffin and OTS⁶ and paraffin and mono-unsaturated alkene.⁸ Paraffin-coated cells were found to preserve the lifetime of spin polarized ^{87}Rb atoms more than OTS-coated cells, and mono-unsaturated alkene-coated cells more than paraffin-coated cells.

We speculate that the ideal cell wall coat would push the destabilized state higher in energy, decreasing the adsorption energy and, consequently, the relaxation rate.

SUPPLEMENTARY MATERIAL

Cartesian coordinates and dipole moments of the MP2/def2-TZVP optimized structures, CASPT2/TZP energy, norm of the electric field, and ground-state electric field gradient with distance for each coat molecule are available in the [supplementary material](#).

ACKNOWLEDGMENTS

We thank T. Mark Fromhold, University of Nottingham, and Mark T. Greenaway, University of Loughborough, for introducing the authors to the interaction of alkali atoms with magnetometer cell wall coatings and for helpful discussions. This research was funded by the University of Nottingham Propulsion Futures Beacon. GD and AMW-T acknowledge the financial support from the European Research Council under the European Union's H2020

research and innovation program/ERC Consolidator Grant topDFT (Grant Agreement No. 772259). We are grateful for the access to the University of Nottingham High Performance Computer.

AUTHOR DECLARATIONS

Conflict of Interest

The authors have no conflicts to disclose.

Author Contributions

Grégoire David: Conceptualization (supporting); Investigation (equal); Methodology (equal); Writing – original draft (supporting); Writing – review & editing (equal). **Andrew M. Wibowo-Teale:** Conceptualization (supporting); Funding acquisition (equal); Methodology (equal); Writing – original draft (supporting); Writing – review & editing (equal). **David M. Rogers:** Conceptualization (lead); Funding acquisition (equal); Investigation (equal); Methodology (equal); Writing – original draft (lead); Writing – review & editing (equal).

DATA AVAILABILITY

The data that support the findings of this study are available within the article and its [supplementary material](#).

REFERENCES

- D. Budker and M. Romalis, "Optical magnetometry," *Nat. Phys.* **3**, 227–234 (2007).
- J. Li, W. Quan, B. Zhou, Z. Wang, J. Lu, Z. Hu, G. Liu, and J. Fang, "Serf atomic magnetometer—recent advances and applications: A review," *IEEE Sens. J.* **18**, 8198–8207 (2018).
- H. Chi, W. Quan, J. Zhang, L. Zhao, and J. Fang, "Advances in anti-relaxation coatings of alkali-metal vapor cells," *Appl. Surf. Sci.* **501**, 143897 (2020).
- Z. Wu, "Wall interactions of spin-polarized atoms," *Rev. Mod. Phys.* **93**, 035006 (2021).
- J. C. Allred, R. N. Lyman, T. W. Kornack, and M. V. Romalis, "High-sensitivity atomic magnetometer unaffected by spin-exchange relaxation," *Phys. Rev. Lett.* **89**, 130801 (2002).
- E. Ulanski and Z. Wu, "Measurement of dwell times of spin polarized rubidium atoms on octadecyltrichlorosilane- and paraffin-coated surfaces," *Appl. Phys. Lett.* **98**, 201115 (2011).
- M. A. Bouchiat and J. Brossel, "Relaxation of optically pumped Rb atoms on paraffin-coated walls," *Phys. Rev.* **147**, 41–54 (1966).
- E. P. Corsini, T. Karaulanov, M. Balabas, and D. Budker, "Hyperfine frequency shift and Zeeman relaxation in alkali-metal-vapor cells with antirelaxation alkene coating," *Phys. Rev. A* **87**, 022901 (2013).
- K. F. Zhao, M. Schaden, and Z. Wu, "Method for measuring surface-interaction parameters of spin-polarized Rb atoms on coated Pyrex glass surfaces using edge enhancement," *Phys. Rev. A* **78**, 034901 (2008).
- S. J. Seltzer, D. J. Michalak, M. H. Donaldson, M. V. Balabas, S. K. Barber, S. L. Bernasek, M.-A. Bouchiat, A. Hexemer, A. M. Hibberd, D. F. J. Kimball, C. Jaye, T. Karaulanov, F. A. Narducci, S. A. Rangwala, H. G. Robinson, A. K. Shmakov, D. L. Voronov, V. V. Yashchuk, A. Pines, and D. Budker, "Investigation of antirelaxation coatings for alkali-metal vapor cells using surface science techniques," *J. Chem. Phys.* **133**, 144703 (2010).
- C. Dong, X. Fang, J. Sang, J. Tang, H. Dong, Y. Sugawara, Y. Li, Z. Ma, and J. Liu, "Energy dissipation during collision for anti-relaxation coatings in alkali-metal vapor cells," *Jpn. J. Appl. Phys.* **61**, 055504 (2022).

- ¹²T. Leininger, A. Nicklass, W. Küchle, H. Stoll, M. Dolg, and A. Bergner, “The accuracy of the pseudopotential approximation: Non-frozen-core effects for spectroscopic constants of alkali fluorides XF (X = K, Rb, Cs),” *Chem. Phys. Lett.* **255**, 274–280 (1996).
- ¹³F. Weigend and R. Ahlrichs, “Balanced basis sets of split valence, triple zeta valence and quadruple zeta valence quality for H to Rn: Design and assessment of accuracy,” *Phys. Chem. Chem. Phys.* **7**, 3297–3305 (2005).
- ¹⁴M. J. Frisch, G. W. Trucks, H. B. Schlegel, G. E. Scuseria, M. A. Robb, J. R. Cheeseman, G. Scalmani, V. Barone, G. A. Petersson, H. Nakatsuji, X. Li, M. Caricato, A. V. Marenich, J. Bloino, B. G. Janesko, R. Gomperts, B. Mennucci, H. P. Hratchian, J. V. Ortiz, A. F. Izmaylov, J. L. Sonnenberg, D. Williams-Young, F. Ding, F. Lipparini, F. Egidi, J. Goings, B. Peng, A. Petrone, T. Henderson, D. Ranasinghe, V. G. Zakrzewski, J. Gao, N. Rega, G. Zheng, W. Liang, M. Hada, M. Ehara, K. Toyota, R. Fukuda, J. Hasegawa, M. Ishida, T. Nakajima, Y. Honda, O. Kitao, H. Nakai, T. Vreven, K. Throssell, J. A. Montgomery, Jr., J. E. Peralta, F. Ogliaro, M. J. Bearpark, J. J. Heyd, E. N. Brothers, K. N. Kudin, V. N. Staroverov, T. A. Keith, R. Kobayashi, J. Normand, K. Raghavachari, A. P. Rendell, J. C. Burant, S. S. Iyengar, J. Tomasi, M. Cossi, J. M. Millam, M. Klene, C. Adamo, R. Cammi, J. W. Ochterski, R. L. Martin, K. Morokuma, O. Farkas, J. B. Foresman, and D. J. Fox, *GAUSSIAN 16, Revision A.03*, Gaussian Inc., Wallingford, CT, 2016.
- ¹⁵I. Fdez Galván, M. Vacher, A. Alavi, C. Angeli, F. Aquilante, J. Autschbach, J. J. Bao, S. I. Bokarev, N. A. Bogdanov, R. K. Carlson, L. F. Chibotaru, J. Creutzberg, N. Dattani, M. G. Delcey, S. S. Dong, A. Dreuw, L. Freitag, L. M. Frutos, L. Gagliardi, F. Gendron, A. Giussani, L. González, G. Grell, M. Guo, C. E. Hoyer, M. Johansson, S. Keller, S. Knecht, G. Kovačević, E. Källman, G. Li Manni, M. Lundberg, Y. Ma, S. Mai, J. P. Malhado, P. Å. Malmqvist, P. Marquetand, S. A. Mewes, J. Norell, M. Olivucci, M. Oppel, Q. M. Phung, K. Pierloot, F. Plasser, M. Reiher, A. M. Sand, I. Schapiro, P. Sharma, C. J. Stein, L. K. Sørensen, D. G. Truhlar, M. Ugandi, L. Ungur, A. Valentini, S. Vancollie, V. Veryazov, O. Weser, T. A. Wesolowski, P.-O. Widmark, S. Wouters, A. Zech, J. P. Zobel, and R. Lindh, “OpenMolcas: From source code to insight,” *J. Chem. Theory Comput.* **15**, 5925–5964 (2019).
- ¹⁶H. Yamamoto and O. Matsuoka, “Accurately energy-optimized Gaussian basis sets for hydrogen 1s through 5g orbitals,” *Bull. Univ. Electro-Commun.* **5**, 23–34 (1992) in Japanese. Citation at <https://ci.nii.ac.jp/naid/40004737908/en/>
- ¹⁷T. Noro, M. Sekiya, and T. Koga, “Correlating basis sets for the h atom and the alkali-metal atoms from Li to Rb,” *Theor. Chem. Acc.: Theory, Comput., Model. (Theor. Chim. Acta)* **109**, 85–90 (2003).
- ¹⁸T. Noro, M. Sekiya, and T. Koga, “Segmented contracted basis sets for atoms H through Xe: Sapporo-(DK)-nZP sets (n = D, T, Q),” *Theor. Chem. Acc.* **131**, 1124 (2012).
- ¹⁹J. Ye, S. Swartz, P. Jungner, and J. L. Hall, “Hyperfine structure and absolute frequency of the ⁸⁷Rb 5P_{3/2} state,” *Opt. Lett.* **21**, 1280–1282 (1996).
- ²⁰G. P. Barwood, P. Gill, and W. R. C. Rowley, “Frequency measurements on optically narrowed Rb-stabilised laser diodes at 780 nm and 795 nm,” *Appl. Phys. B: Photophys. Laser Chem.* **53**, 142–147 (1991).